Raman modes in Pbca enstatite (Mg2Si2O6): An assignment by quantum mechanical calculation to interpret experimental results

Published version:

DOI:10.1002/jrs.4942

Stangarone, Claudia; Tribaudino, Mario; Prencipe, Mauro; Lottici, Pier Paolo.
Raman modes in Pbca enstatite (Mg2Si2O6): An assignment by quantum mechanical calculation to interpret experimental results. JOURNAL OF RAMAN SPECTROSCOPY. None pp: 1-12.
DOI: 10.1002/jrs.4942

Raman modes in *Pbca* enstatite ($Mg_2Si_2O_6$): an assignment by quantum mechanical calculation to interpret experimental results

Claudia STANGARONE[1], Mario TRIBAUDINO[1], Mauro PRENCIPE[2], Pier Paolo LOTTICI[1]

[1] Dipartimento di Fisica e Scienze della Terra "Macedonio Melloni",

Università di Parma, Parco Area delle Scienze, 157/A, 43124 Parma, Italy

[2] Dipartimento di Scienze della Terra, Università di Torino,

Via Valperga Caluso, 35, 10125 Torino, Italy

Keywords: Orthoenstatite, pyroxenes, experimental vs calculated spectra, Ab initio HF/DFT calculation

Abstract

Raman spectra of orthoenstatite have been computed from first principles, employing the hybrid Hamiltonian WC1LYP [1]. The calculated data show excellent agreement with the experimental data from literature with an absolute average difference of ~5 cm^{-1}. The quantum mechanical simulation allowed the assignment of Raman features to specific vibrational modes. This enabled to assess quantitatively the contributions of internal (tetrahedral stretching) and external (tetrahedral chains and M1 and M2 cations) vibrations. Moreover, the mass substitution of ^{56}Fe for ^{24}Mg in the M1 and M2 sites and of ^{30}Si and ^{18}O for the ^{28}Si and ^{16}O sites, pointed out the relative contributions of the cations to each mode within different sites.

The description of the Raman modes enabled to relate the major experimental peaks to specific structural vibrations, and to link the changes in crystal structure to those of the mode frequencies with pressure, temperature and composition.

The results provide new clues to identify most suitable peaks for the investigation of the intracrystalline ordering of Fe and Mg in the M1 and M2 sites, and of Al in the tetrahedral and octahedral sites. Moreover we have been able to identify those peaks which are related to structural features, like tetrahedral bond distances.

Introduction

Enstatite (Mg_2Si_2O6) is an endmember and a major component of natural pyroxenes. Enstatite forms a solid solution series with ferrosilite (Fe_2Si_2O6) in the mineral orthopyroxene (space group P*bca*), which is a rock forming mineral in mafic and ultramafic assemblages of the Earth crust and upper mantle. Moreover, enstatite is an important constituent of other planetary bodies and meteorites, where a specific class of undifferentiated chondrites takes its name (enstatite chondrites). It is also one of the few silicate minerals that was observed in crystalline form outside our Solar System, around evolved stars and planetary nebulae [2]. In addition, the enstatite phases are important constituents of steatite ceramics [3].

Enstatite displays a complex polymorphism. Although the orthorhombic phase is the most common, monoclinic $P2_1/c$ clinoenstatite is also found at room temperature, both as a quenched metastable product and as a stable phase below 700℃. At non ambient conditions, clinoenstatite transforms in the high pressure and high temperature HP$C2/c$ and HT$C2/c$ phases, sharing the same space group, but with quite different structure [4]; orthoenstatite transforms in the *Pbcn* protoenstatite at high temperature and low pressure [5] and in a HP$P2_1/c$ phase at high pressure[6, 7, 8]. Phase transitions between the enstatite phases have a considerable importance in the thermodynamic and geophysical behaviour of the upper mantle; relations between different polymorphs, their structure, and their vibrational properties have been therefore widely investigated, at room conditions and at high pressure and temperature [9].

Extensive spectroscopic studies were performed on enstatite; among spectroscopic methods, micro-Raman has a special interest, since it analyses on a micrometer scale the polymorphic varieties of enstatite, often mixed together, providing an effective tool for their identification [10].

Raman spectroscopy has been applied not only as tool to discriminate between clino-, ortho- and protoenstatite [3,10] but also to probe the chemical composition of orthoenstatite-orthoferrosilite solid solutions (orthopyroxenes) providing means to determine the orthopyroxene composition [11, 12, 13]. The high temperature and high pressure phase transitions were also investigated by Raman [14,7,8], and detailed spectra at non ambient conditions were collected to describe the high pressure and high temperature mode behaviours [15, 16]. Moreover, a number of studies exploited Raman spectroscopy to identify the enstatite phases in rocks and meteorites [17].

The Raman spectra of clino and orthoenstatite were also simulated by numerical modelling. A pioneering study was performed by Choudhury [18], who calculated the Raman peak positions of orthoenstatite by means of molecular dynamics, comparing the results with carefully determined experimental spectra in parallel and cross polarization. However, due to the limitation in molecular dynamics, the difference between calculated and experimental positions was quite large (up to 100

cm^{-1}). A more precise fit to the experimental results was determined by DFT quantum mechanical investigations: where Raman peak positions of ortho- and clinoenstatite were calculated as a by-product of calculations of the energetics and stabilities of the different polymorphs [19]. Although these calculations are in closer agreement with experimental data, peak intensities were not computed. In fact, the high number of allowed Raman peaks (120 in orthoenstatite) makes peak assignment a challenging task, due to overlapping peaks. Therefore, calculation of the intensities is required to provide a correct assignment, i.e. to link a given experimental peak to a calculated one. Most recently, within the Wurm project [20], DFT modelling was performed systematically over a series of mineral families; intensities and peak positions were calculated and reported for ortho and clino enstatite, however the results were not object of further study. Among the DFT based calculations, the thermodynamic properties and phase transition of $MgSiO_3$ at high pressure were calculated in a pure GGA simulation [21].

Here we discuss the results of new simulations of Raman spectra of orthoenstatite from first principles, by means of CRYSTAL14 [22], employing the hybrid Hamiltonian WC1LYP [1], which is particularly suitable to calculate vibrational frequencies, as demonstrated for *C*2/*c* pyroxenes, like diopside, jadeite and spodumene [23, 24, 25] and in the -1 plagioclase albite [26]. Full Raman spectra are simulated, and the peak assignment is discussed in comparison with computational and experimental literature; the contribution of each atom to the vibration is assessed performing a building unit decomposition of the vibrational modes and by means of isotopic substitutions. Last, the specific changes of the crystal structure with Fe-Mg substitution, temperature and pressure have been related to the orthoenstatite Raman modes, to enlighten major structural features affecting the changes in Raman peak positions.

The results, compared with the available literature data, will provide the basis to model details in Raman peak changes with composition and cation ordering in natural samples.

Computational details

To simulate the Raman spectra of orthoenstatite from first principles, the following algorithm was used: 1) Solve the ground-state wave functions; 2) perform the calculation of the corresponding energies at the static limit, i.e. not taking into accounts the zero point and thermal energies [27]; 3) calculate vibrational frequencies and the complete analytical calculation of the second order Raman tensor after the optimization of the crystal structure. All calculations were performed with CRYSTAL code, which employs localized Gaussian-type basis sets and hybrid Hamiltonian.

The contracted basis sets used are 8-511d1G for Mg, 88-31G* for Si and 8-411d11G for O. The chosen Hamiltonian (WC1LYP) was a hybrid HF/DFT one, based on the generalized gradient approximation (GGA) exchange functional WC, proposed by Wu and Cohen [1], mixed with 16% of the exact non-local Hartree-Fock exchange, and employing the LYP correlation functional proposed by Lee [28]. Such percentage of exact Hartree-Fock exchange is essential for the correct reproduction of the elastic and vibrational properties, as demonstrated in previous works that employ these hybrid functionals [24, 29-34].

Geometry optimization is conducted by analytical gradient methods, optimizing cell parameters and fractional coordinates. The equilibrium lattice parameters optimized by CRYSTAL are here reported in **Table 1** and compared with the experimental data [5].

Vibrational wavenumbers and normal modes were calculated within the limit of the harmonic approximation, by diagonalizing a mass weighted Hessian matrix, whose elements are the second derivatives of the full potential of the crystal with respect to mass weighted atomic displacements. The first derivatives of the energy with respect to the atomic positions are calculated analytically [35], whereas second derivatives are calculated numerically by setting to 0.003 Å the nuclear displacements with respect to the equilibrium positions.

Relative Raman intensities were computed using a fully analytical approach. It combines analytical gradients [35] with solutions of first-order and second-order coupled perturbed Hartree–Fock/Kohn–Sham equations [36] for the linear and quadratic orbital responses to electric fields in the different Cartesian directions. For the linear response, there are three directions to consider, whilst for the quadratic response, there are six pairs corresponding to the six independent components of the polarizability tensor. The thresholds for convergence of the coupled perturbed equations were set to the default values. The diagonalization of the Hessian matrix was performed at six independent k vectors in the reciprocal space (Monkhorst net).

Full spectra were calculated for a polycrystalline orthoenstatite powder and for a single crystal in different orientation and polarization, (see Fig. S1 for the latter, Fig. 2 for the former). All the comparisons and the analysis of the most characteristic modes are referred to the unpolarised polycrystalline powder spectrum, which can be easily compared with the experimental data from literature as shows Fig. 2. In Tables 1 the experimental data of orthoenstatite from previous works are compared with our calculated ones. The comparison was carried out using both the peak positions and their intensities.

Results

Mode analysis

The orthoenstatite Raman spectrum is one of the most complex in pyroxenes, being the result of as much as 120 Raman active modes; it can be described batter comparing it with other enstatite polymorphs and their structure.

Pyroxenes are chain silicates, with tetrahedral chains along the c axis, and two metal sites (M1 and M2) in between. The M1 site is located in a slightly distorted octahedron, whereas the M2 is an irregular polyhedron, hosting cations in six and eightfold coordination. In *Pbca* enstatite, Mg cations occupy both the M1 and the M2 sites in six-fold coordination (see Fig. 1). In *C*2/*c* pyroxenes, the M2 polyhedron is eightfold, and hosts cations with ionic radius higher than Mg, like Ca and Na. The different coordination requirements promote a change in the tetrahedral chains arrangement. In *C*2/*c* pyroxenes, the chains are symmetry equivalent, whereas in the monoclinic $P2_1/c$ symmetry, they are not, since the chains are distorted differently, which means that they are divided into two of the four tetrahedral chains. The orthorhombic enstatite occurs by twinning of the P21/c unit cell, leading to a Pbca symmetry and a doubled unit cell volume. Like in the $P2_1/c$, in the *Pbca* enstatite there are two symmetry independent chains.

Orthoenstatite has eight formula units ($Mg_2Si_2O_6$) per unit cell, i.e. 80 atoms requiring 240 vibrations (3n, where n is number of atoms per unit cell). At the centre of the Brillouin zone, the symmetry assignment of the 240 normal modes of orthoenstatite is:

$$\Gamma = 30A_g + 30B_{1g} + 30B_{2g} + 30B_{3g} + 30A_{1u} + 30B_{1u} + 30B_{2u} + 30B_{3u}$$

There are therefore 120 Raman active modes ($30B_{1g}$, $30B_{2g}$, $30B_{3g}$ and 30 A_g), 87 IR active modes ($29B_{1u}$, $29B_{2u}$ and $29B_{3u}$), 30 ‘silent’ A_u modes; three modes corresponding to pure translations have B_{1u}, B_{2u} and B_{3u} symmetry.

In *C*2/*c* pyroxenes factor group analysis gives rise to 30 Raman active modes: most can be experimentally identified, in polarized light experiments [23, 37]. In the $P2_1/c$ symmetry, we have 60 Raman active modes, of which 30 can be observed in parallel polarization (A_g) and 30 in cross polarization (B_g).

The unit cell, doubled in *Pbca* orthoenstatite, doubles also the number of the modes. The A_g symmetry modes are the most intense and useful for the purpose of mineral identification and spectroscopic analysis: unpolarised spectrum consists almost completely of A_g modes (Fig. 2). The B_g modes are generally weaker and can be identified by the analysis of spectra in cross polarization configuration [18, 38]. However, the high number of modes hinders a careful experimental analysis due to overlap in close peaks. In addition, the simple description of the modes in terms of definite structural vibrations is difficult: the pyroxene structure has little crystallographic constrains, due to its low symmetry, and allows significant polyhedral deformation. In their investigation on polarized spectra of orthoenstatite, Choudhury [18] managed to measure and to identify successfully all the A_g and some of the B_{1g} and B_{3g} modes, but none of the B_{2g}.

In previous papers [11, 12, 18] three different kind of vibrations were identified: 1) vibration of cations in M1 and M2 polyhedron, occurring with varying contribution from the tetrahedral chains; 2) bending of the tetrahedral chains, involving both or one of the two symmetry equivalent chains; 3) stretching into the SiO_4 tetrahedron, with minor contribution from the M1 and M2 cations. They were identified to specific group of wavenumbers, i.e. group 1 for wavenumbers between 200 and 400 cm^{-1}, group 2 between 400 and 800 cm^{-1}, and tetrahedral stretching to higher wavenumbers. However, although the above assignment can provide a preliminary information, mode assignment is more complex, since previous quantum mechanical investigation on the *C*2/*c* pyroxenes showed that a combination of the above vibrations might contribute to the same mode [24, 33]. As described in the following, it has little meaning to say that a mode is due e.g. to M1-O bending, as long as it will likely have a significant contribution in bending and stretching from the tetrahedral chain. Instead, the description of a given mode should enlighten the prevailing mechanism, and account for the different contributions.

To unravel the different contributions of the atomic vibrations, we have performed a building unit decomposition of the vibrational modes: they are decomposed in terms of internal and external motions of some defined units. The external motions correspond to rotations and translations of the units behaving as rigid blocks, while the internal motions to the relative movements of the constitutive atoms. In pyroxenes, the internal contributions come from the bending or stretching of the tetrahedral units, while the external contribution comes from the vibration of the tetrahedral chains without an internal deformation; the vibrations of the M2 and M1 atoms fall in the range of the external contribution. The results, in terms of numbers and percentages are summarized in Table 3.

The contribution of a given atom to the overall vibration was also assessed by means of isotopic substitution of Fe atomic mass for Mg mass in the M2 and M1 sites, separately and together, and of ^{18}O and ^{30}Si isotopes for the oxygen and silicon respectively. These calculations are activated by the keyword ISOTOPES, which allows the modification of the atomic mass of a specific atom defined by input. With ISOTOPES calculations, the atomic mass of one atom can be modified, without any modification of the electronic wave function or geometry optimization, since the mass of the atoms are not present in the single particle electronic Hamiltonian. Moreover, if a frequency calculation was performed with standard atomic masses, new frequencies values with different atomic masses for selected atoms can be computed from the Hessian already computed. This has the advantage to separate the contributions due to the changing mass of the vibrating atoms, with those from the interatomic force constants. The choice of the much heavier Fe mass, instead of a Mg isotope, was performed in order to assess the mass contribution for the Fe-Mg substitution in the Raman spectra of enstatite-ferrosilite orthopyroxenes.

The contributions of the building units from enstatite can be found for each vibrational mode in Table 3.

In the following general trends are discussed, in order to identify the vibrational behaviour prevailing in a given wavenumber range.

Building unit decomposition

As expected from the results in *C*2/*c* clinopyroxenes [23], we find that also for orthopyroxene most modes are a combination of internal and external contributions (Fig. 3 and 4, Table 3). Internal contributions are most at higher wavenumbers, where they account almost completely for the description of the Raman mode intensities, and decrease with decreasing wavenumbers. This is quite similar for A_g and B_g vibrations. The external contribution is complementary, but it must be further divided into tetrahedral vibrations contribution and Mg in the M1 and M2 sites vibration.

Within the internal contribution (Fig. 3) five ranges can be identified, that we also reported in Fig. 2, where ranges are reported as R1 to R5: 1) below 150 cm^{-1}, where the internal contribution is less than 10%; 2) between 150 and 350 cm^{-1} where it is below 20%; 3) between 350 and 600 cm^{-1} where it linearly increases between 20 to more than 80%; 4) between 600 to 800 cm^{-1}, where it is between 75 and 80% and 5) for higher energy wavenumbers where it is more than 80%. Purely internal contribution is never found (Table 3).

Tetrahedral contribution dominates the overall vibration from wavenumbers above 750 cm^{-1}. A contribution of Mg in M1 and M2 atoms is present at the lower wavenumbers, mostly between 200 and 400 cm^{-1}, but tetrahedral internal and external contributions generally prevail.

M1 and M2 isotopic substitution

The isotopic substitution of Fe in the M1 and M2 sites induces a downshift of the peak positions for modes below 760 cm^{-1} (Fig. 4).

In the substitution of Fe for Mg in the M1 site, the downshifting is maximum at 250 cm^{-1}; between 250 to 400 cm^{-1} the wavenumber downshifts by an amount between 20 and 40 cm^{-1}. The downshifting is lower at higher wavenumbers and is not present for wavenumbers higher than 760 cm^{-1}. The same substitution for the M2 site shows a similar trend, but with the maximum shift observed in few modes at lower energy, at about 200 cm^{-1}.

The complete Fe isotopic substitution in M2 and M1 sites decreases the wavenumber by 40 to 60 cm^{-1} between 200 to 400 cm^{-1}. The maximum downshift increases up to 200 cm^{-1} and decreases from 400 to 760 cm^{-1}, showing a pronounced linear trend.

Si and O isotopic substitution

The isotopic substitution was calculated for each of the two Si atoms of A and B chains separately and for each of the six symmetry independent oxygens; eight separate calculations were performed (more explanation are given in Fig. S2 and S3.

Oxygen isotopic substitution downshifts the wavenumbers for most modes, whereas the Si isotopic substitution affects significantly the calculated wavenumbers only above 600 cm^{-1}. In fact, oxygens are involved also in vibration due to the M1/M2-O, even if the internal tetrahedral contributions are less significant. The isotopic substitution changes the wavenumbers by more than 5 cm^{-1} only for the O1A and B and the O2A and B, for some modes between 400 and 600 cm^{-1} and above 900 cm^{-1}, and for the O3A and B, between 600 and 900 cm^{-1}. At wavenumbers higher than 900 cm^{-1} the contribution for the O1 and O2 atoms is maximal, especially O2 oxygens at the highest wavenumbers, whereas the O3 contribution becomes not significant.

Discussion

Peaks assignment

Combining the results of isotopic substitution and building units decomposition, we outlined the prevailing vibrational pattern for each wavenumber range. Details for each range can be found in Table 3 where we analyse the more intense and diagnostic peaks, reported by Lin [15], compared with our calculated data. Moreover, the motion has been described by means of the graphic interface software Moldraw (http://www.moldraw.unito.it/_sgg/f10000.htm), which implements the vibrational pattern of each mode, by analysing the eigenvectors.

The range defined as (R1) is from 79 cm^{-1}, first mode, to 150 cm^{-1}. It shows stiff external lattice movements, without an internal deformation of tetrahedra. The mode with the highest intensity in this group is found at 79 cm^{-1} (A_g), where tetrahedra oscillate stiffly along the b axis and where the contribution of chain A prevails; here both Mg cations are dragged by tetrahedra, but at a greater extent for the Mg in the M2 site. This mode has often been overlooked as most Raman spectra have been measured from 100 cm^{-1}, but it is diagnostic for the identification of the orthopyroxene phase

[2]. The motion for the mode at 127 cm^{-1} (A_g) is rather similar to the one at 79 cm^{-1}, but here the contribution of the B chain is predominant. Modes at 81 cm^{-1} and 108 cm^{-1} are respectively of B_{2g} and B_{3g} symmetry, as reported by Lin [13]. They are again stiff lattice oscillations, where chains vibrate onto the (001) plane. At higher wavenumbers, the vibration of Mg in the M2 sites becomes significant.

In the second range (R2) we recognized two subranges:

a) from 150 to 300 cm^{-1}, where M2 contributions are predominant with respect to other cations. The peak with higher M2 contribution is at 248 cm^{-1} (B_{2g}). In this range, both chains are involved in the vibration, but the motion can be different for the two chains. For example at 206 cm^{-1} (A_g), the A chain performs a Si-O3-Si bending, whereas the B chain swings rigidly onto the (001) plane. On the other hand it has been observed that at 161 cm^{-1} (B_{1g}), 236 cm^{-1} (A_g) and 277 cm^{-1} (A_g), the chains vibrate with the same tilting motion along the a axis, but with a different percentage;

b) in the second subrange, from 300 to 350 cm^{-1}, the contribution of Mg in the M1 site increases consistently, reaching its maximum at about 325 cm^{-1} (A_g). Here the B chain is almost stationary and the A chain vibrates for the bending of the O2 atom with Mg in the M2 site. There is also a contribution of the internal deformations of the tetrahedra (Table 3). The most intense peak in our unpolarised calculated spectra is the one at 343 cm^{-1} (A_g), where the motion is characterized by the tilting of both tetrahedral chains, due to O1 and O2 vibrations. Both the M2 and M1 cations vibrate, but the isotopic contribution from the M2-O vibration is higher.

The range between 350-600 cm^{-1} (R3) is characterized by an almost equal percentage of both rigid movements of the lattice and internal strains of the tetrahedra. The contribution from the internal tetrahedral vibration increases steeply and, in some modes, the isotopic contribution from the oxygens may be significant. In this range a lower but significant contribution from the M1 and, to a lesser extent, from M2 is still present. Also here the range can be further divided into two sub-ranges: a first one (R3a) between 350 and 470 cm^{-1}, with balanced internal and external contribution, and a second one (R3b), where the internal contribution begins to prevail and the contribution of the M2 and M1 cations starts to decrease gradually. The R3a range is characterized by low intensity doublets and triplets (see Fig. 2), whereas in R3b few peaks are measured experimentally. In the R3a subrange both chains vibrate, but with different movements and the vibration of Mg in the M1 site gives the highest contribution. The triplet consisting of three A_g modes at 387 cm^{-1}, 406 cm^{-1} and 426 cm^{-1} is noteworthy. The motion of the chains for the first mode is a prevailing stretching of O1 inside the A tetrahedron; for the second mode both chains vibrate, O1 oxygen swinging along the a axis in the B chain and the tetrahedra tilting above and below the b axis. For the last mode of the triplet, at 426 cm^{-1}, the vibration involves both chains, but more the A chain, where the motion of tetrahedra is mainly due to the O1 oxygen. In general, in the R3 range, analysing the oxygen mass substitution, it seems that most of the contribution to the vibration comes for O1 and O2 atoms, i.e. those having shorter bonds with M1 and M2 cations, respectively. In the second subrange (R3b) few significant peaks experimentally observed,are present. An exception is the one at 594 cm^{-1} (B_{1g}) which was ascribed to a O2-Si-O1 bending in the A chain combined by the vibration of the O2 together with the two Mg in M1 and M2.

A fourth range (R4) in the spectrum occurs between 600 and 760 cm^{-1}, where the most intense peaks are those at 660 and 680 cm^{-1}, both A_g modes. This range was defined as bending zone [11], where the contribution to the overall vibration consists of internal vibrations of the tetrahedra, with the characteristic bending of O3-Si-O3. The peak at 660 and 680 cm^{-1} shows different contributions from the A and B chains.

In a fifth range (R5) the M2 and M1 cations contribution is less than 1%. The modes in this final part of the spectrum are characterized by internal strains of the tetrahedra, and by a different contribution of the two chains to the overall vibration. This range can be further divided in two subranges. Within R5a, modes are characterized with a higher contribution from the O3 oxygen, the most intense is the A_g mode at 866 cm^{-1} and the doublet, not very intense, consisting of two A_g modes at 924 cm^{-1} and 933 cm^{-1}. For R5b subrange, the higher contribution comes from Si-O1 and O2 stretching within the tetrahedron. In this last subrange, we find the final triplet at wavenumbers higher than 1000 cm^{-1}, which is described as symmetric and asymmetric stretching of Si-O within the tetrahedra.

The above observations can be easily related in terms of bond distances and crystal chemical requirements (Table S1). The average bond distances are longer in the M1 and M2 polyhedra than in the Si centred tetrahedra: it means that the modes with higher contribution from the M1 and M2 sites are the ones with the lower wavenumber. The same goes within the tetrahedron bond distances: the Si-O3 distances are the longest and the Si-O3 stretching modes are those with the lower energy among Si-O stretching modes. The high intensity and high wavenumber A_g doublet at 1012 cm^{-1} and 1027 cm^{-1} is most related to Si-O2 vibrations and the Si-O2 distances are the shortest in the tetrahedron.

In terms of crystal chemistry [39 - 42] the O3 oxygens are overbonded, since they are bridging between tetrahedra and receive their charge contribution from the two Si atoms and the M2 atoms, whereas the O2 and, less, the O1 are underbonded. Tetrahedral bond distances change consequently and a change in the reduced mass for O1 and O2 promotes a higher shift in the highest energy modes. Moreover, only the O1 and O2 atoms are bonded to the M1 cations (Fig S2b), which accounts for the contribution in some modes between 350-500 cm^{-1} of the O1 and O2 oxygens, but not of the O3. The contribution of the O3 to the modes involving the M2 and M1 atoms is quite small, since they are the chain bridging atoms. In fact their contribution to the vibration becomes significant in modes related to chain bending within the 600-700 cm^{-1} range.

Fe-Mg substitution and orthopyroxene composition by Raman spectroscopy

In the partial substitution of Fe^{2+} for Mg^{2+} both cations have the same charge, therefore the space group does not change along the whole composition range of the solid solution series enstatite-ferrosilite. Fe^{2+} has a higher mass and a larger size than Mg^{2+}, thus Mg and Fe do not enter randomly the two cationic site M1 and M2, but Fe enters preferentially the more distorted (and slightly larger) M2 polyhedron. [43].

The intracrystalline distribution coefficient: $K_D = [Fe_{M1}]*[Mg_{M2}]/[Fe_{M2}]*[Mg_{M1}]$ is temperature dependent [44-46], and varies in volcanic and metamorphic orthopyroxenes between 0.2 to 0.02. It is an important marker for the cooling history in meteoritics, volcanics and slowly cooled terranes [47-49].

In Fig. 5, we report the Raman shift vs composition of several peaks along the $Mg_2Si_2O_6$ - $Fe_2Si_2O_6$ series. The expectation is that the increased mass of Fe decreases the energy of the modes, at least those where a significant contribution from the M1 and M2 cation exists. This is observed for the peaks up to 800 cm^{-1}, but the experimentally measured peak wavenumbers decrease with Fe content more than calculated by simple isotopic substitution of Fe with the lighter Mg. Actually, the mode wavenumbers depend not only on the mass, but also on the force constants, which are in turn related to the bonding type and bond lengths. The higher ionic radius of Fe promotes longer bond lengths and lower coulombic contributions to the oxygen bonding (Table S1): it promotes a further contribution to decrease the energy of the modes when Fe exchanges for Mg. Apparently the contribution from mass, which can be modelled by our isotopic substitutions (Fig. 4), and that for the changing structure, are comparable (Fig. 5).

The above considerations do not hold for modes at higher wavenumbers (> 800 cm^{-1}), which are ascribed to the internal vibrations of the tetrahedra. Actually, the peaks at 866 and 933 cm^{-1} do show an increase in wavenumbers with Fe content, whereas the peak at 1010 cm^{-1} shows higher wavenumbers in Mg richer orthopyroxenes. Again, changes in tetrahedral bond distances along the $Mg_2Si_2O_6$-$Fe_2Si_2O_6$ series, must be taken into account. In orthoenstatite endmember the two O1 and O2 atoms are closely bound to Si, whereas the O3-Si bridging oxygen distances are longer. As Fe increases, the bond distances in the tetrahedron come closer together: the distance of Si with the O3 decreases, while O1 and O2 increase (Table S1) [50]. To note, on average, the tetrahedral size does not change. As shown by isotopic substitution in Fig. 4 the modes at 866 and 933 cm^{-1} are most affected by the O3 atomic vibrations, and, decreasing the Si-O3 bond distance with increasing Fe, it is not surprising that the mode wavenumber increases too. The mode at 1010 cm^{-1}, mainly due to vibrations involving O2, coherently decreases its wavenumber with the increasing Si-O bond distance, according to an higher content of Fe.

Isotopic analysis predicts also that Fe-Mg ordering can have a significant effect on Raman peak positions. In natural intermediate orthopyroxenes Fe is almost completely confined into the M2 site, and Mg in the M1 site [47]; Fe occupies at a larger extent the M1 site only in Fe richer orthopyroxenes. In the isotopic modelling of the partitioning between M1 and M2, the configuration in which Mg fully occupies the M1 site, is an ordered model, close to the experimental observation, whereas when Fe occupies M1 and Mg M2, is an anti-ordered one. According to our calculations in most of the modes the discrepancy between the ordered and anti-ordered models is very small (Fig. 6), but in the relatively strong peak at 302 cm^{-1} a marked difference between ordered and anti-ordered configuration is found. This mode could be a candidate to reveal differences within Fe-Mg ordering, since the substitution of Fe in M1 downshifts the peak much more than that of Fe in M2. The few experimental available data for the peak at 302 cm^{-1} can be better fitted in the ordered model (Fig. 5), confirming that the mode at 302 cm-1 is a potential probe for Fe-Mg intracrystalline ordering. At the author knowledge, no experimental investigation was performed to verify the effect of Fe-Mg cation ordering on Raman active modes. According to changes among the degree of cation ordering in orthopyroxenes, a sensitive peak was found by Tarantino [45], by means of IR spectroscopy technique.

Among of other important cation substitutions in orthopyroxenes, like the Ca for Mg into M2 site and Al for Mg and Si into M1 and T sites, there is a lack of Raman experimental data on orthopyroxenes with such solid solutions. However with this approach we can provide some suggestion on the expectable changes. For instance, the entrance of Al into the tetrahedral sites will mostly affect the tetrahedral stretching modes at higher wavenumber, reducing their frequency wavenumber, as Al increases the tetrahedral bond distances [53, 54]. Instead, the entrance of Al in the M1 site will affect the modes involved with M1 vibrations: we can foresee that an increasing amount of Al goes into the M1 site, which has shorter bonding, higher charge and lower mass and therefore can shift the vibrations more affected by the M1 site to higher energy. Although Raman data on natural Al-rich orthopyroxenes are also lacking, the presence of tetrahedral Al is expected to be experimentally significant. In *C*2/*c* pyroxenes, the highest energy peak at 1010 cm^{-1} in diopside decreases to 953 cm^{-1} in the Ca-Tschermak pyroxene ($CaAl_2SiO_6$), where half of the tetrahedral sites are occupied by Al [55]. Likewise, we can expect that the Ca for Mg exchange downshifts the wavenumber of the peak related to the M2 site vibration. In fact this effect was observed, beyond the effect of phase transitions, in the $CaMgSi_2O_6$-$Mg_2Si_2O_6$ pyroxenes [51].

Raman modes and structure: relations with HP/HT Raman behaviour

The above discussion shows that changing mass and bond parameters provide a clue to interpret and, potentially, predict the mode behaviour in response to changing composition, once the mode assignment has been performed correctly. Furthermore, this approach can be extended conveniently to analyse the behaviour of HP/HT Raman modes in comparison with HP/HT structural data. For this purpose, enstatite is a good candidate, since a number of in situ high quality single crystal XRD data are available and only bond distances are modified by pressure and temperature changing. Here we just take into account high temperature/pressure behaviour of the doublet at 664/686 cm^{-1}, here calculated at 668/693 cm^{-1} (Fig.6), which is intense and well resolved, and therefore potentially useful for diagnostic purposes [11, 17, 51].

The doublet at 664/686 cm^{-1} is described as a bending of the tetrahedral chains [9]. However, according to our calculations performed with isotopic substitution (Fig. 4), a contribution from M1 and M2 atoms is also present. The split of the doublet occurs as only one of the two symmetry independent tetrahedral chains is in turn involved in the mode vibrations: the mode at 664 cm^{-1} involves a vibration of the B chain, whereas that at 686 cm^{-1}, the A chain. In *C*2/*c* pyroxenes a single mode at 670 cm^{-1} is present, and the transition from C to P pyroxenes is marked by the peak split at 664/686 cm^{-1} of the formerly unique peak at 665 cm^{-1} [50, 51]. The higher energy of the vibration from the A chain can be explained taking into account the tetrahedral bond distances. In fact within the tetrahedron, Si A bond distances are shorter than the Si B (on average 1.629 vs 1.640 Å and in particular the O3 bridging oxygen, which most contributes within this vibration 1.653 vs 1.675 Å). Moreover, the shorter distance between M1 and any atom of the tetrahedral chain, i.e. the M1-O2 distance, is less between M1-O2A than between M1-O2B (2.001 vs 2.053 Å). This distance, which is the shortest between M1/M2 cations, together with tetrahedral oxygens, is supposed to affect significantly the tetrahedral chain vibration.

In Fig. 7 we plotted the wavenumbers of the peaks at 664/686 cm^{-1} *vs* the bond distance of the shorter M1-O2 distance in the M1 polyhedron (a) and *vs* the average T-O distance (b). The plot was carried out with the M1-O2a and average TA-O distances for the peak at 686 cm^{-1} and with the M1-O2b and average TB-O distances for the peak at 664 cm^{-1}. The peak positions were also plotted *vs* the O3-O3-O3 kinking angle (c), a parameter that is expected to vary with intra-chain kinking, i.e. chain bending. Each of the Raman data in Fig. 7 was plotted against structural parameters taken at the same experimental conditions: every point corresponds to a given P-T condition. The Raman peak positions at high pressure and temperature were interpolated from Lin [15] and Zucker [16] to the P-T conditions of the *in situ* single crystal measurements [52]. A single linear trend with pressure and temperature is clearly observed with the M1-O distances; the same could be observed, but with higher dispersion of the data points, from the average tetrahedral bond distance (Fig. 8 a and b). The larger distribution likely comes from the higher relative experimental uncertainty in structural determination, in turn due to lower changes in bond distances with pressure and temperature in the tetrahedron. On the contrary, the O3-O3-O3 chain kinking shows separate trends for the A and B chains (Fig. 7c). It appears therefore that the mode changes are determined mostly by bonding with the M1 cation and by intratetrahedral stretching, rather than by the chain rotation. We can therefore expect that these modes, quite strong and well measureable, will be very sensitive to any structural substitution in the M1 site.

Conclusion

The simulation of the Raman spectrum provided by combined DFT with a Hartree-Fock exchange contribution is very close to the experimental spectrum, both in peak position and intensities. It shows that quantum mechanical modelling can be used to interpret the observed experimental spectra and find links between crystal structure and spectroscopic feature. Going further, the simulation provides a theoretical framework in which is possible to model the observed spectra, especially in those complex cases such as orthoenstatite.

We have shown that quantum mechanical calculations, combined with a careful description of the modes and exploiting some zero computational cost tools of CRYSTAL14 (i.e. isotopic substitution or building units decomposition), enable to assess the influence of bond distances and cation masses on a given mode. Therefore, we can assume that there are modes which can be defined sensitive, whose wavenumbers are related to the structural changes with pressure, temperature and composition.

On the other hand, atomic masses and bond distances are related to the composition and provide a clue for the most significant modes, which can lead to a specific cation substitution, within structural sites. For instance, we have found that in the peak at 866 cm^{-1}, even relatively minor changes in the tetrahedral bond distances, (T-O3) between enstatite and ferrosilite, promote significant changes in Raman peak positions. This again, can be related to atomic composition, for instance Fe-Mg or Al-Si content, and makes Raman spectroscopy a probe for a site specific compositional determination, i.e. a probe for intracrystalline ordering.

We believe that our approach of combining experimental structural data and *ab initio* quantum mechanical calculation can be employed also in other minerals and mineral families, providing theoretical basis and hints for future experimental Raman investigations and applications to mineral sciences.

Acknowledgments

The authors wish to acknowlwdge Ronald Stalder and three anonymous reviewers for their accurate review and constructive criticism. Ronald Stalder is also thanked for sending the original files for orthoenstatite.

References

[1] Z. Wu and R.E. Cohen, *Phys. Rev. B*, **2006**; 73, 235116.

[2] R. Demichelis, B. Civalleri, M. Ferrabone, R. Dovesi, R.: *Int. J. Quantum Chem.* **2010**; 110, 406-415.

[3] B. Reynard, D. Bass Jay, J. M. Jackson, *J. Eur. Ceram. Soc.* **2008**; 28, 2459-2462.

[4] R. J. Angel, A. Chopelas, N. L. Ross, *Nature,* **1992**; 358, 322-324.

[5] H. Yang, & S. Ghose, *Phys. Chem. Miner*. **1995**; 22(5), 300-310.

[6] J. S. Zhang et al., *Am. Mineral*. **1997**; 1070–1074

[7] J. S. Zhang, B. Reynard, G. Montagnac, R. C. Wang, J. D. *Am. Mineral*. **2013**; 98(5-6), 986-992.

[8] J. S. Zhang, B. Reynard, G. Montagnac, G., J. D. Bass, *Phys. Earth Planet. Inter.* **2014**; 228, 150-159.

[9] R. J. Angel, & J. M. Jackson, *Am. Mineral*. **2002**; 87(4), 558-561.

[10] P. Ulmer and R. Stalder, *Am. Mineral.* **2001**; 86, 1267–1274.

[11] E. Huang, C. H. Chen, T. Huang, E. H. Lin, J. A. Xu, *Am. Mineral.* **2000**; 85, 473-479.

[12] A. Wang, B. L. Jolliff, L. A. Haskin, K. E. Kuebler, K. M. Viskupic, *Am. Mineral.* **2001**; 86, 790–806.

[13] R. Stalder, A. Kronz, and B. C. Schmidt, *Eur. J. Mineral*. **2009**; 21, 27-32.

[14] N. L.Ross & B. Reynard, *Eur. J. Mineral*. **1999**; 11, 585-589.

[15] C. C. Lin, *J. . Solids State Chem.***2003**; 65(5), 913-921.

[16] R. Zucker, & S. H. Shim, *Am. Mineral.* **2009**; *94*(11-12), 1638-1646.

[17] A. Wang, K. Kuebler, B. L. Jolliff, L. A. Haskin, *J. Raman Spectrosc.* **2004**; 35, 504-514

[18] N. Choudhury, S. Ghose, C. P. Chowdhury, C. K. Loong, S. L. Chaplot, *Phys. Rev. B: Solid State* **1998**; 58 756-765

[19] Y. G. Yu & R. M. Wentzcovitch, *Am. Mineral.* **2009**; 94(4), 461-466.

[20] R. Caracas, E. Bobocioiu, *Am. Mineral* **2011**; 96, 437–443.

[21] B. Li, J. Kung, W. Liu, R. C. Liebermann, *Phys. Earth. Planet. Interi* **2013;** 228, 63-74.

[22] R. Dovesi, V. R. Saunders, C. Roetti, R. Orlando, C. Zicovich-Wilson, F. Pascale, B. Civalleri, K. Doll, N. M. Harrison, I. J. Bush, P. D'Arco, M. Llunell, M. Causà, Y. Noël, *CRYSTAL14 User's Manual*, University of Torino, Torino, **2014**.

[23] M. Prencipe, L. Mantovani, M. Tribaudino, D. Bersani, P.P. Lottici P.P. *Eur. J. Mineral.* **2012**; 24, 457-464

[24] M. Prencipe, L. Maschio, B. Kirtman, S. Salustro, A. Erba, R. Dovesi, *J. Raman Spectrosc.* **2014**; 45(8), 703-709.

[25] C. Stangarone, M. Prencipe, L. Mantovani, D. Bersani, M. Tribaudino, P. P. Lottici, 11th International GeoRaman Conference, **2014** St. Louis, Missouri. *LPI Contribution .n. 1783, id. 5061*

[26] I. Aliatis, E. Lambruschi, L. Mantovani, D. Bersani, S. Andò, D. G. Gatta, P. Gentile, E. Salvioli-Mariani, M. Prencipe, M. Tribaudino, P. P. Lottici, J. Raman Spectrosc. **2015**; 46(5), 501-508.

[27] M. Prencipe, I. Scanavino, F. Nestola, M. Merlini, B. Civalleri, M. Bruno, R. Dovesi, *Phys. Chem. Miner.* **2011**; 38, 223-239.

[28] C. Lee, W. Yang, R. G. Parr, *Phys. Rev. B* **1988**; 37, 785–789

[29] C. M. Zicovich-Wilson, F. Pascale, C. Roetti, V. R. Saunders, R. Orlando, R. Dovesi, *Comput. Chem.* **2004**; 25, 1873-1881.

[30] C. G. Ungureanu, M. Prencipe, R. Cossio, *Eur. J. Mineral*. **2010**; 22, 693-701.

[31] C. G. Ungureanu, R. Cossio, M. Prencipe, M. *Calphad* **2012**; 37, 25-33.

[32] M. De La Pierre, R. Orlando, L. Maschio, K. Doll, P. Ugliengo, R. Dovesi, *J. Comput. Chem.* **2011**; 32, 1775-1784

[33] M. Prencipe, *J. Raman Spectrosc*. **2012**; 43(11), 1567-1569.

[34] I. Scanavino, R. Belousov, M. Prencipe, *Phys. Chem. Miner.* **2012**; 39 649-663

[35] K. Doll, V. R. Saunders & N. M. Harrison, *Int. J. Quantum Chem.* **2001**; 82(1), 1-1

[36] M. Ferrero, M. Rérat, R. Orlando, R. Dovesi, *J. Comput. Chem*. **2008**; 29(9), 1450-1459.

[37] J. Etchepare, *Amorphous materials International Conference on Noncrystalline Solids, Wiley Interscience, London*, **1972**; 337-346.

[38] A. Chopelas, *Am. Mineral.* **1999**; *84*, 233-244

[39] M. Cameron, S. Sueno, C. T. Prewitt, J. J. Papike, *Am. Mineral.* **1973**; 58, 594-618

[40] L. Mantovani, M. Tribaudino, F. Mezzadri, G. Calestani, G. Bromiley, *Am. Mineral.* **2013**; 98, 1241-1252.

[41] L. Mantovani, M. Tribaudino, G. Bertoni, G. Salviati, G. Bromiley, *Am. Mineral*. **2014**; 99, 704-711.

[42] C. Gori, M. Tribaudino, L. Mantovani, D. Delmonte, F. Mezzadri, E. Gilioli, G. Calestani, *Am. Mineral.* **2015**; 100, 2209-2218

[43] M. C. Domeneghetti, G. M. Molin, V. Tazzoli, *Am. Mineral*. **1985**; 70, 987-995

[44] S. C. Tarantino, T. Boffa Ballaran, M. A. Carpenter, M. C. Domeneghetti, V. Tazzoli, *Eur. J. Mineral.* **2002**; 14, 525-536

[45] S. C. Tarantino, T. Boffa Ballaran, M. A. Carpenter, M. C. Domeneghetti, V. Tazzoli, *Eur. J. Mineral.* **2002**; 14, 537-547

[46] L. Wang, N. Moon, Y. Zhang, W. R. Dunham, E. J. Essene, *Geochim. Cosmochim. Acta*, **2005**; 69, 5777–5788

[47] M. Tribaudino, F. Talarico, *Eur. J. Mineral*. **1992**; 4, 453-463.

[48] M. C. Domeneghetti, G. M. Molin, M. Stimpfl, M. Tribaudino, *Am. Mineral.* **1995**; 80, 923-929

[49] M. Stimpfl, J. Ganguly, G. M. Molin, *Contrib. Mineral. Petrol*. **2005**; 150, 319-334

[50] L. Mantovani, M. Tribaudino, I. Aliatis, E. Lambruschi, D. Bersani, P. P. Lottici, *Phys. Chem. Miner*. **2015**; 42, 179-189.

[51] M. Tribaudino, L. Mantovani, D. Bersani, P. P. Lottici, *Am. Mineral.* **2012**; 97(8-9), 1339-1347.

[52] B. Periotto, T. Balić-Žunić, F. Nestola, A. Katerinopoulou, R. J. Angel, *Am. Mineral.* **2012**; 97, 1741-1748.

[53] F. P. Okamura, S. Ghose, H. Ohashi, *Am. Mineral.* **1974**; 59, 549-557

[54] M. Tribaudino. *Eur. J. Mineral.* **1996**; 8, 273-279.

[55] S. K. Sharma, B. Simons, H. S. Yoder, Am. Mineral. **1983**; 68, 1113-1125

Tables

Table 1: Experimental and calculated structural parameters. The bond distances are average values.

	Yang e Ghose (1995) (Å)	**This work (Å)**
a	18.21	18.285
b	8.812	8.864
c	5.178	5.225
V	830.896 Å^3	846.8 Å^3
<M2-O>	2.152	2.161
<M1-O>	2.077	2.087
<SiA-O>	1.629	1.640
<SiB-O>	1.641	1.651

Table 2: Comparison between the 120 calculated Raman peak positions and the experimental data from literature**.** Δν is the difference between ν calculated (this work) and experimental (from literature). In the statistics given at the bottom of the table, *N* is the number of peaks considered, <|Δ|> is the mean absolute difference, in wavenumber, and max Δν is the maximum absolute difference, min Δν is the minimum absolute difference. In the Lin spectrum, the intensities are classified as strong *s*, medium *m*, weak *w* and shoulder *h*.

This work		**Lin, 2003**			**Stalder et al. 2009**		**Chopelas 1999**		**Zhang et al. 2013**	
ν cm^{-1}	**Symm**	**ν cm^{-1}**	**I**	**Δν**	**ν cm^{-1}**	**Δν**	**ν cm^{-1}**	**Δν**	**ν cm^{-1}**	**Δν**
79	**(A_g)**	83	s	-4			83	-4		
81	**(B_{2g})**	106.8	w	-26						
108	**(B_{3g})**	115.4	w	-8			115	-7		
127	**(A_g)**	134.3	ms	-7	133.8	-6.8	134	-7	137.4	-10
159	**(A_g)**	155.3	wm	4			153	6		
161	**(B_{1g})**	161.5	vw	-1						
166	**(B_{3g})**	166.7	w	-1			166	0	170.2	-4
184	**(B_{1g})**								190.1	-6
195	**(B_{1g})**	196.9	wm	-2	197.5	-2.6	197	-2	196.5	-2
201	**(A_g)**								201.1	0
206	**(A_g)**	206.5	wsh	-1	206.4	-0.5			208.3	-2
236	**(A_g)**	238.2	ms	-2	239	-2.7	237	-1	240.1	-4
238	**(B_{2g})**						239	-1	241.1	-4
248	**(B_{2g})**	244.8	msh	3			245	3	246.3	2
270	**(A_g)**						261	9	260.8	9
277	**(A_g)**	278.2	w	-1					271.6	6
296	**(B_{3g})**								286.5	10
305	**(A_g)**	301.5	w	3	302.5	2.3	302	3	303.2	2
325	**(A_g)**	323.3	wsh	2						
327	**(B_{3g})**	327.7		-1						
341	**(B_{2g})**								340.3	1
341	**(B_{1g})**								342.9	-2
343	**(A_g)**	343.5	svs	0	343.9	-0.5	343	0	345.4	-2
379	**(B_{1g})**								374	5
387	**(A_g)**	383.8	wm	3	385.2	1.9			381	6
406	**(A_g)**	402.1	m	4	402.8	3.5	402	4	402.6	4
426	**(A_g)**	421.7	m	4	422.7	2.9	422	4	424.2	1
451	**(A_g)**	445.5	w	6	445.9	5.5	446	5	445.4	6
458	**(B_{1g})**								448	10
458	**(A_g)**	458.8	vw	0			457	1	458.6	0
474	**(B_{2g})**	472.9	vw	1					478.7	-5
481	**(A_g)**						487	-6	488.3	-7
536	**(A_g)**	524.9	m	11	527	8.6	519	17	528.1	7
542	**(B_{3g})**				540.8	0.9	540	2	541.9	0
552	**(A_g)**	551.5	m	0	553.5	-1.5	553	-1	554.5	-3

566	**(B$_{3g}$)**	580.3	m	-14			580	-14	582.1	-16
594	**(B$_{1g}$)**	594.5	vw	-1	581	13.0				
668	**(A$_g$)**	663.8	svs	5	664.8	3.6	665	3	664.9	4
693	**(A$_g$)**	686.1	vs	7	687.1	5.7	687	6	687.7	5
760	**(B$_{2g}$)**	750.7	w	9					752.7	7
866	**(A$_g$)**	851.1	m	15	853.2	12.6	886	-20	851	15
924	**(A$_g$)**	926.6	m	-2	927.9	-3.4	927	-3	929.6	-5
933	**(A$_g$)**	935.2	w	-2	936.5	-3.1	937	-4		
1012	**(A$_g$)**	1011.3	vs	0	1013.2	-1.6	1014	-2		
1027	**(A$_g$)**	1032.9	svs	-6						
1039	**(A$_g$)**				1034.7	4.7	1034	5		
<|Δ|>				5		4		5		5
max Δν				-26		13		-20		15.8
min Δν				0		0		0		0.0

Tab 3: building unit decomposition of the vibrational modes: they are decomposed in terms of internal (INT) and external (EXT) motions of some defined units. The external motions correspond to rotations and translations of the units behaving as rigid blocks, while the internal motions to the relative movements of the constitutive atoms. For a) and b) column, refer to Fig. 2

	Calculated	**Symmetry**	**Motion**		**int+ext contribution of T**		**Tetrahedra vibration**		**Cations**		
	ν (cm^{-1})		**EXT**	**INT**	**chain A**	**chain B**	**A int**	**B int**	**M1**	**M2**	
Range 1	79	(A_g)	98.2	1.8	59.5	16.7	0.2	1.6	9.4	14.5	
	81	(B_{2g})	98.6	1.4	77.4	4.8	0.2	1.1	6.7	11.0	
	108	(B_{3g})	97.5	2.6	23.6	59.2	0.4	2.2	2.4	14.8	
	127	(A_g)	96.5	3.5	17.0	77.5	0.4	3.1	0.9	4.6	
Range 2	159	(A_g)	94.6	5.4	80.5	10.4	4.2	1.2	5.8	3.4	**a)**
	161	(B_{1g})	96.3	3.7	58.6	32.5	2.2	1.4	4.6	4.2	
	166	(B_{3g})	89.9	10.1	52.2	18.2	5.0	5.2	15.0	14.5	
	195	(B_{1g})	98.8	1.2	24.6	57.3	1.0	0.2	1.1	17.0	
	206	(A_g)	98.3	1.7	49.2	24.6	0.7	1.0	1.7	24.5	
	236	(A_g)	91.0	9.0	24.6	57.8	2.0	7.0	13.8	3.8	
	248	(B_{2g})	85.7	14.3	29.2	21.2	6.9	7.4	11.0	38.6	
	277	(A_g)	89.2	10.8	20.3	53.1	1.4	9.4	10.2	16.3	
	305	(A_g)	78.3	21.7	35.6	26.3	7.4	14.3	28.4	9.7	**b)**
	325	(A_g)	81.3	18.7	37.8	9.8	13.8	5.0	46.2	6.1	
	327	(B_{3g})	79.2	20.8	31.9	16.2	13.0	7.8	43.0	8.7	
	343	(A_g)	87.1	12.9	39.8	49.4	5.4	7.5	3.4	7.3	
Range 3	387	(A_g)	63.9	36.1	39.8	40.6	20.6	15.5	16.9	2.9	**a)**
	406	(A_g)	59.1	40.9	40.2	39.8	22.2	18.7	12.5	7.5	
	426	(A_g)	40.0	60.0	55.0	31.4	34.2	25.8	10.0	3.5	
	451	(A_g)	58.7	41.3	30.6	50.1	17.7	23.7	10.6	8.7	
	458	(A_g)	55.3	44.7	66.6	14.5	35.6	9.2	17.5	1.4	
	474	(B_{2g})	24.9	75.1	49.0	41.8	37.6	37.5	6.6	2.4	
	536	(A_g)	15.9	84.1	12.6	83.0	11.0	73.1	2.2	2.1	**b)**
	552	(A_g)	14.6	85.5	37.9	54.6	32.2	53.3	3.8	3.7	
	566	(B_{3g})	22.3	77.7	32.6	50.5	30.9	46.9	4.2	12.8	
	594	(B_{1g})	16.1	83.9	88.5	3.3	81.8	2.1	3.7	4.6	
Range 4	668	(A_g)	27.1	72.9	2.1	89.6	2.0	71.0	3.9	4.4	
	693	(A_g)	21.0	79.0	90.9	2.1	77.2	1.8	3.7	3.4	
	760	(B_{2g})	17.0	83.0	26.3	73.0	21.9	61.0	0.3	0.5	
Range 5	866	(A_g)	14.2	85.8	0.1	99.9	0.1	85.7	0.0	0.0	**a)**

	924	(A_g)	10.7	89.3	67.4	31.6	58.4	31.0	0.4	0.5	
	933	(A_g)	10.6	89.4	67.4	32.2	57.9	31.5	0.2	0.3	
	1012	(A_g)	6.5	93.5	61.6	37.7	58.2	35.2	0.2	0.4	**b)**
	1027	(A_g)	4.1	95.9	9.6	90.2	9.0	86.8	0.1	0.1	
	1039	(A_g)	4.5	95.5	94.3	5.5	90.3	5.1	0.2	0.1	

Table S1: all the 120 Raman vibrational modes calculate for orthoenstatite. Frequencies and intensities have been calculated with CRYSTALcode.

Wavenumber (cm^{-1})	symmetry	Intensity	Wavenumber (cm^{-1})	symmetry	Intensity
78.6	(A_g)	702.37	152.8	(B_{1g})	0.18
127.0	(A_g)	146.72	160.7	(B_{1g})	8.18
159.4	(A_g)	37.55	184.3	(B_{1g})	4.75
193.4	(A_g)	15.65	194.9	(B_{1g})	65.02
201.3	(A_g)	16.55	224.1	(B_{1g})	14.85
205.9	(A_g)	13.70	245.2	(B_{1g})	15.00
236.3	(A_g)	100.91	282.9	(B_{1g})	5.69
269.7	(A_g)	16.17	457.5	(B_{1g})	0.00
277.3	(A_g)	33.49	468.0	(B_{1g})	32.62
425.6	(A_g)	142.09	488.6	(B_{1g})	1.74
451.4	(A_g)	49.03	522.3	(B_{1g})	3.21
458.4	(A_g)	6.17	531.3	(B_{1g})	7.79
481.2	(A_g)	9.66	594.0	(B_{1g})	55.37
535.6	(A_g)	64.27	610.2	(B_{1g})	14.87
552.0	(A_g)	79.78	299.1	(B_{1g})	3.01
561.5	(A_g)	19.32	310.7	(B_{1g})	1.61
668.4	(A_g)	621.25	340.9	(B_{1g})	10.77
304.8	(A_g)	100.47	347.7	(B_{1g})	12.05
325.1	(A_g)	138.92	379.0	(B_{1g})	0.21
335.6	(A_g)	13.99	394.5	(B_{1g})	1.44
343.4	(A_g)	1000.00	406.4	(B_{1g})	15.50
387.1	(A_g)	137.92	422.2	(B_{1g})	24.42
406.3	(A_g)	236.20	735.3	(B_{1g})	1.08
692.8	(A_g)	666.19	758.7	(B_{1g})	0.24
865.8	(A_g)	18.24	885.9	(B_{1g})	3.77
924.5	(A_g)	28.83	918.7	(B_{1g})	0.25
933.4	(A_g)	115.13	945.0	(B_{1g})	0.42
1011.6	(A_g)	590.85	1023.3	(B_{1g})	4.37
1026.7	(A_g)	653.31	1043.4	(B_{1g})	19.74
1039.4	(A_g)	204.55	1066.6	(B_{1g})	1.67

Wavenumber (cm^{-1})	symmetry	Intensity	Wavenumber (cm^{-1})	symmetry	Intensity
81.2	(B_{2g})	4.75	107.7	(B_{3g})	66.54
160.0	(B_{2g})	0.00	145.1	(B_{3g})	3.85
163.9	(B_{2g})	7.11	158.1	(B_{3g})	22.88
212.0	(B_{2g})	0.24	166.1	(B_{3g})	5.44
237.5	(B_{2g})	44.51	195.6	(B_{3g})	0.34
248.2	(B_{2g})	119.94	224.7	(B_{3g})	1.76
426.5	(B_{2g})	9.92	233.4	(B_{3g})	4.07
448.8	(B_{2g})	2.65	263.0	(B_{3g})	2.39
473.9	(B_{2g})	10.52	450.2	(B_{3g})	0.59
477.4	(B_{2g})	2.85	469.6	(B_{3g})	8.51
498.4	(B_{2g})	2.21	523.4	(B_{3g})	7.38
527.2	(B_{2g})	23.42	541.7	(B_{3g})	8.00
553.2	(B_{2g})	19.18	549.7	(B_{3g})	8.52
609.8	(B_{2g})	3.85	566.3	(B_{3g})	0.11
285.0	(B_{2g})	6.17	658.8	(B_{3g})	2.34
303.5	(B_{2g})	0.09	296.2	(B_{3g})	0.53
311.2	(B_{2g})	16.97	298.8	(B_{3g})	5.05
340.8	(B_{2g})	4.23	318.3	(B_{3g})	23.72
359.0	(B_{2g})	18.79	326.6	(B_{3g})	2.70
388.6	(B_{2g})	29.09	364.0	(B_{3g})	2.43
401.1	(B_{2g})	2.84	386.4	(B_{3g})	0.75
414.7	(B_{2g})	1.33	412.1	(B_{3g})	6.54
748.8	(B_{2g})	6.21	421.7	(B_{3g})	4.68
760.0	(B_{2g})	12.44	688.0	(B_{3g})	0.00
893.9	(B_{2g})	1.69	865.7	(B_{3g})	11.63
906.1	(B_{2g})	2.81	931.7	(B_{3g})	10.14
942.8	(B_{2g})	0.50	957.2	(B_{3g})	0.97
1016.7	(B_{2g})	18.41	1023.8	(B_{3g})	7.32
1025.1	(B_{2g})	8.74	1026.4	(B_{3g})	6.84
1062.6	(B_{2g})	9.11	1152.5	(B_{3g})	0.07

Tab. S2: experimental bond distances in orthoenstatite and orthoferrosilite from literature.

	(Yang & Ghose) $M_{g2}Si_2O_6$ **(Å)**	**(Sasaki et al. 1992)** $Fe_2Si_2O_6$ **(Å)**
M1-O1A	2.025	2.086
-O1A	2.153	2.193
-O2A	2.005	2.128
-O1B	2.065	2.195
-O1B	2.172	2.085
-O2B	2.042	2.122
mean	2.077	2.135
M2-O1A	2.090	2.090
-O2A	2.037	2.037
-O3A	2.287	2.287
-O1B	2.056	2.056
-O2B	1.994	1.994
-O3B	2.448	2.448
mean	2.152	2.152
SiA-O1A	1.614	1.612
-O2A	1.590	1.604
-O3A	1.646	1.636
-O3A	1.667	1.652
mean	1.629	1.626
SiB-O1B	1.623	1.619
-O2B	1.589	1.603
-O3B	1.674	1.663
-O3B	1.679	1.667
mean	1.641	1.638

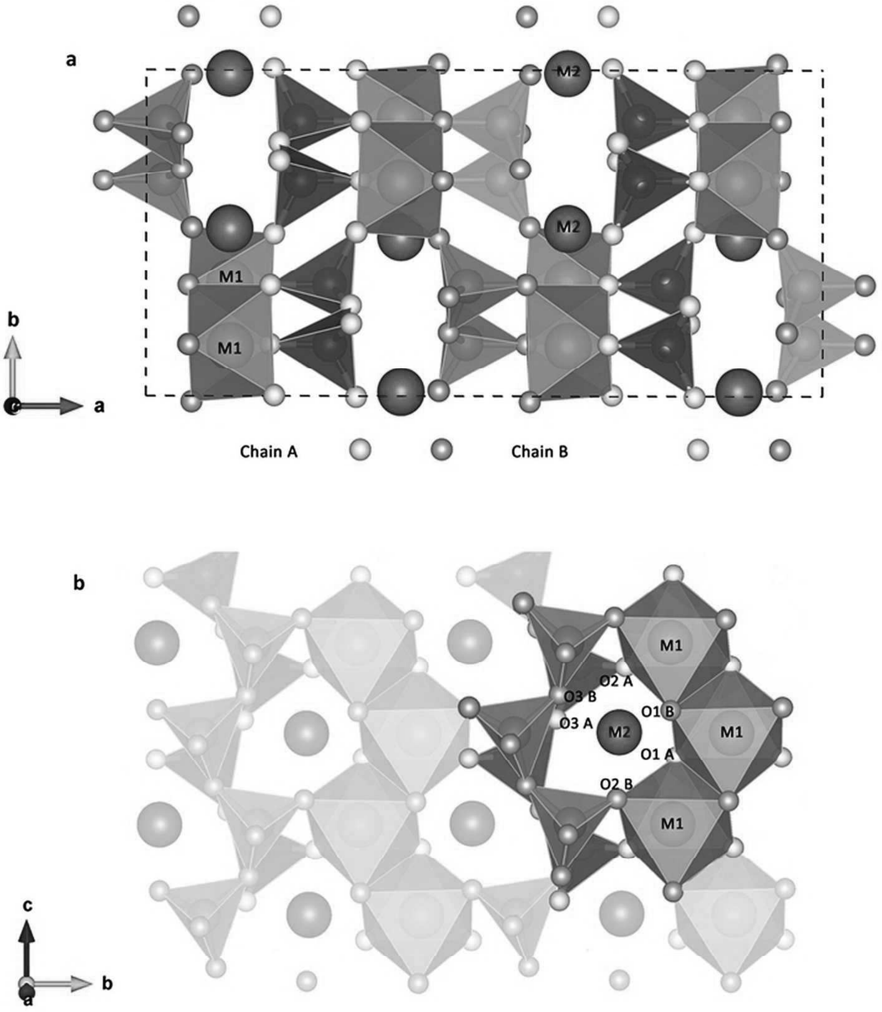

Fig. 1: View of the Pbca structure of orthoenstatite, along the [001] axis (a) and along the direction normal to it (b): the different bonds of the two Mg cations with the oxygens from A and B chains can be distinguished. The two tetrahedral chains have been coloured differently: blue for the A chain, pink for the B chain.
133x148mm (300 x 300 DPI)

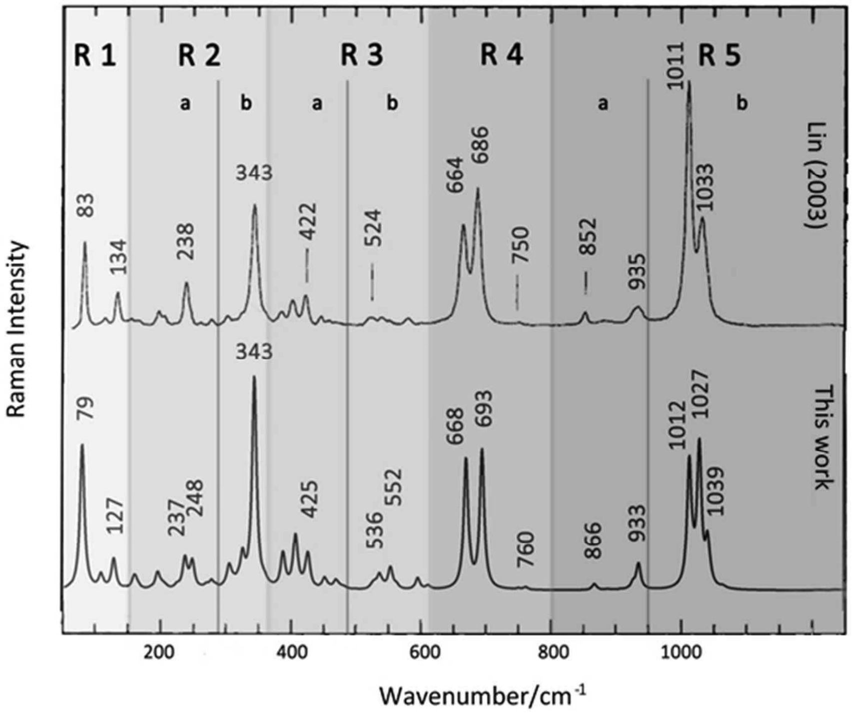

Fig. 2: Comparison between the experimental [13] (top) and calculated (bottom) non-polarized spectrum of orthoenstatite. The Raman pattern has been divided into 5 ranges (R1 to R5) and 6 subranges (a and b), following the discussion in the text.
55x42mm (300 x 300 DPI)

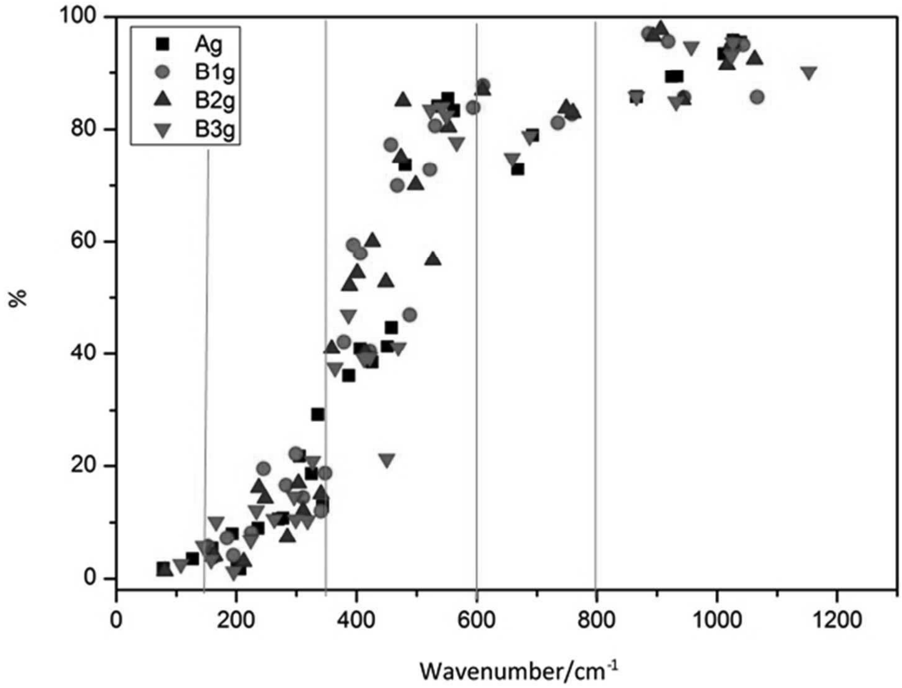

Fig. 3: It has been performed a building unit decomposition of the vibrational modes: they are decomposed in terms of *internal* and *external* motions of some defined units. Quantitatives details are listed in Table 3. Here we plot the contribution of the internal tetrahedral vibrations to the overall vibration for each mode. All the 120 Raman active modes have been considered. In pyroxenes, the internal contributions come from the bending or stretching of the tetrahedral units, while the external contribution comes from the vibration of the tetrahedral chains without an internal deformation.
240x184mm (72 x 72 DPI)

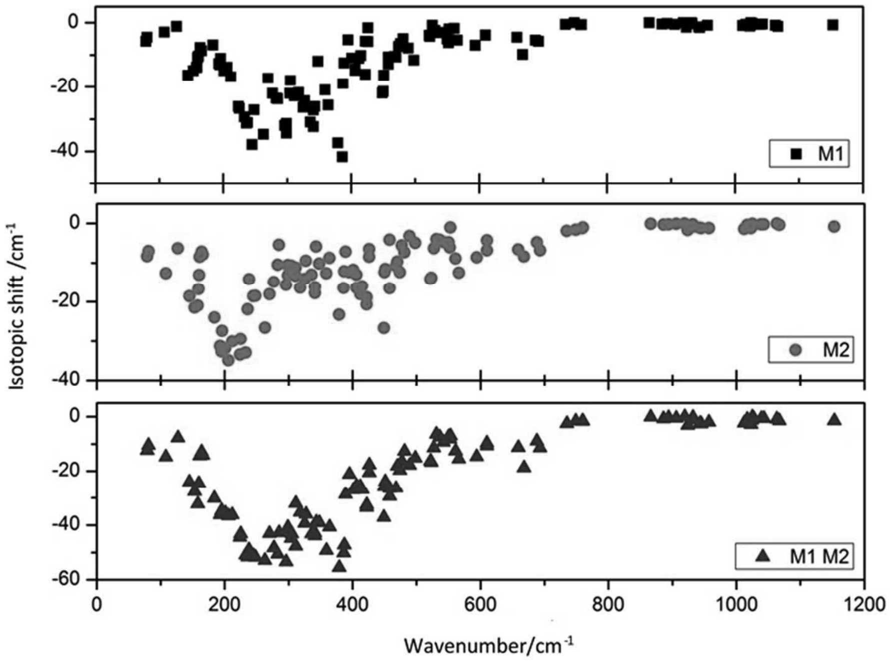

Fig. 4: Shift of the Raman wavenumbers for the isotopic substitution of an atom with the mass of ^{56}Fe for Mg, in M1, M2 and M1+M2 sites. All the 120 Raman active modes have been considered, as in Fig. 3.
283x207mm (72 x 72 DPI)

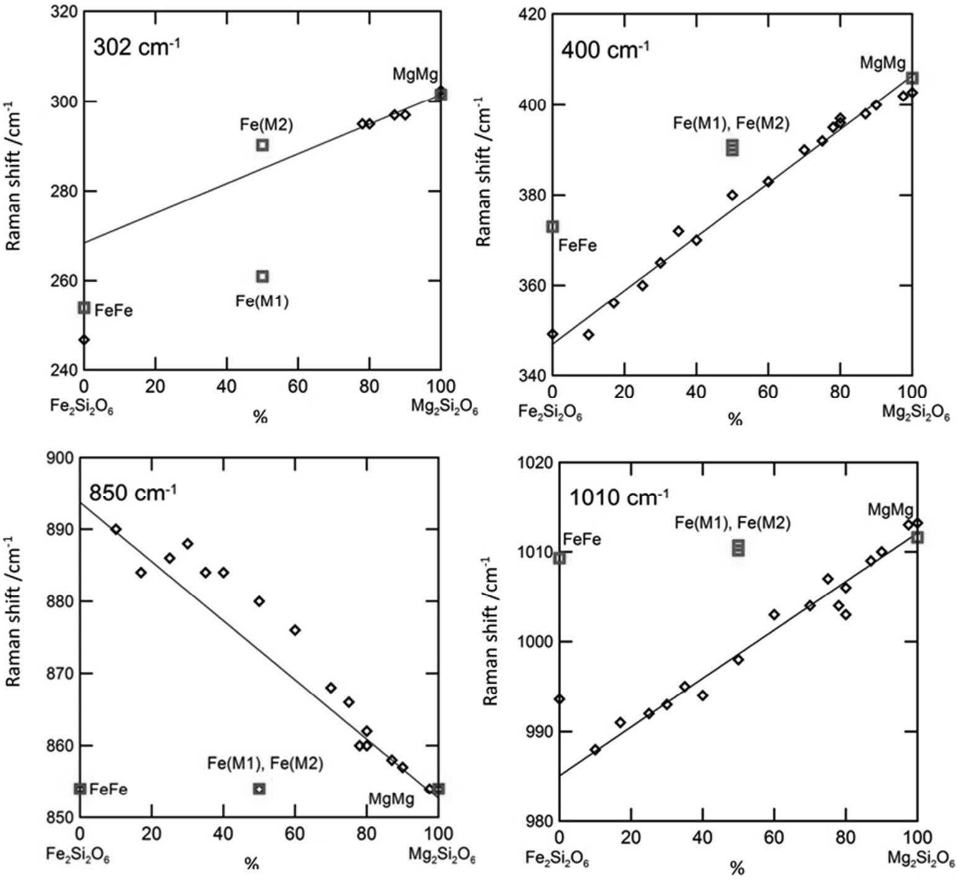

Fig. 5: Raman shift vs composition of several modes along the $Mg_2Si_2O_6$ - $Fe_2Si_2O_6$ series. Squares are the results of mass substitution; diamonds are experimental Raman data [9].
300x274mm (72 x 72 DPI)

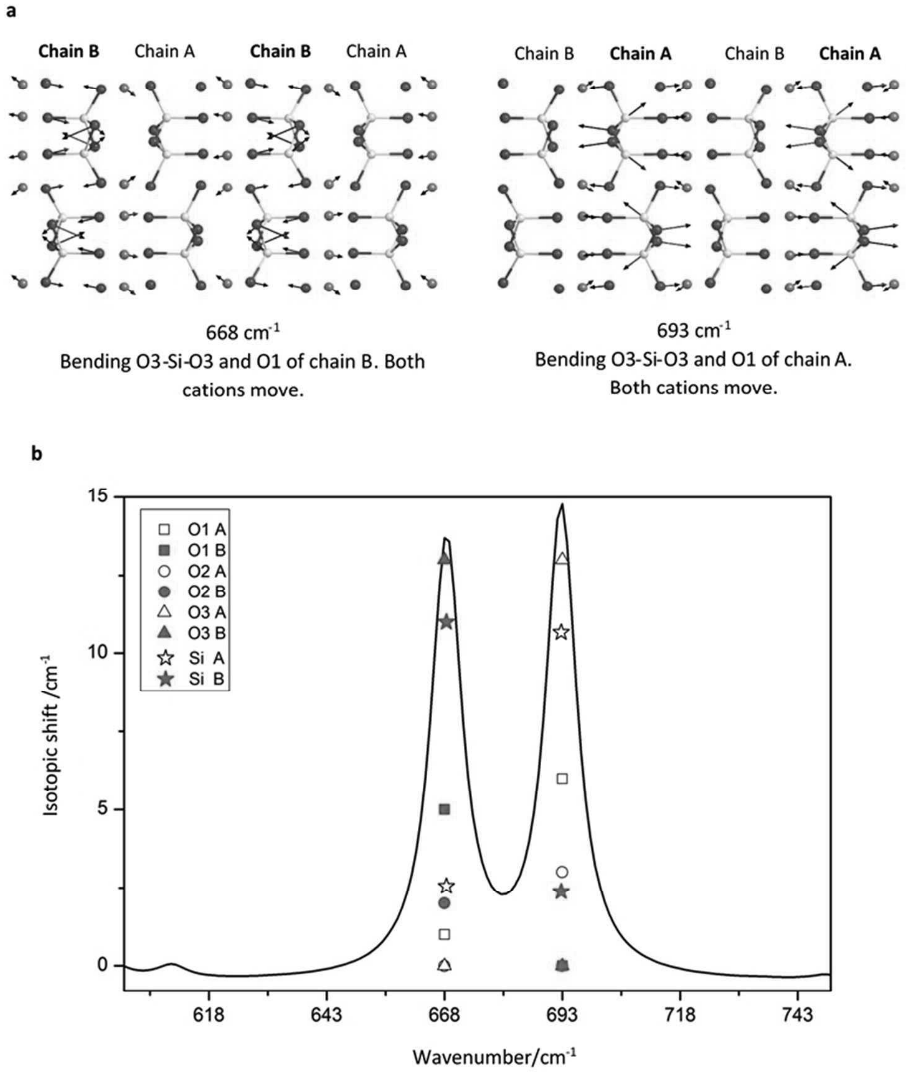

668 cm^{-1}
Bending O3-Si-O3 and O1 of chain B. Both cations move.

693 cm^{-1}
Bending O3-Si-O3 and O1 of chain A. Both cations move.

Fig. 6: a) graphical representation of the vibrations for the modes at 668 and 693 cm^{-1} on [001] plane; b) detailed isotopic contribution for the split modes at 668 and 693 cm^{-1}.
292x330mm (72 x 72 DPI)

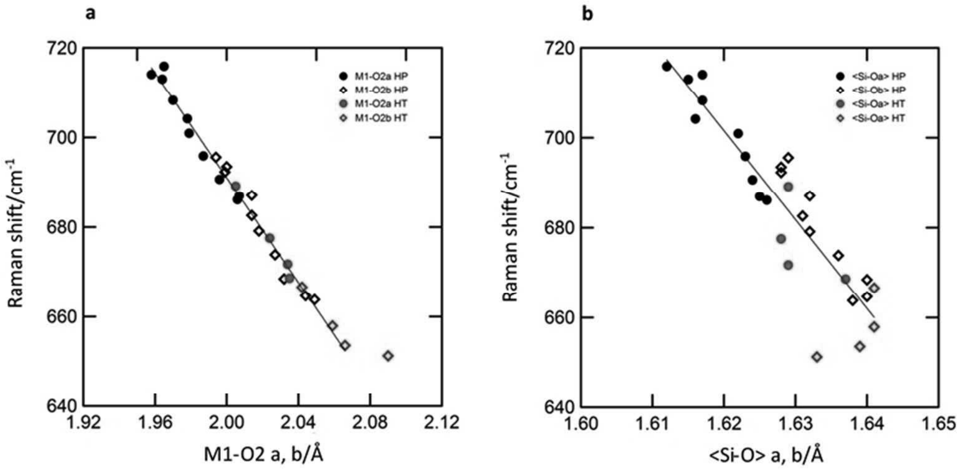

Fig. 7: Raman shift and bond distances and angles for the peaks at 664-686 cm^{-1} with pressure and temperature in orthoenstatite. a) Raman shift vs M1-O2a, b bond distances; b) Raman shift vs <Si-O> a, b tetrahedral distances.
69x35mm (300 x 300 DPI)